Please cite the Published Version

Hubert, McKenzie A, Gallo, Alessandro, Liu, Yunzhi, Valle, Eduardo, Sanchez, Joel, Sokaras, Dimosthenis, Sinclair, Robert, King, Laurie A and Jaramillo, Thomas F (2022) Characterization of a Dynamic Y2Ir2O7 Catalyst during the Oxygen Evolution Reaction in Acid. The Journal of Physical Chemistry C, 126 (4). pp. 1751-1760. ISSN 1932-7447

DOI: https://doi.org/10.1021/acs.jpcc.1c07760

Publisher: American Chemical Society (ACS)

Version: Accepted Version

Characterization of a Dynamic $Y_2Ir_2O_7$ Catalyst During the Oxygen Evolution Reaction in Acid

McKenzie A. Hubert,[a] Alessandro Gallo,*[,b] Yunzhi Liu,[c] Eduardo Valle,[a] Joel Sanchez,[a] Dimosthenis Sokaras,[d] Robert Sinclair,[c] Laurie A. King,*[,e] Thomas F. Jaramillo*[,a,b]

[a] SUNCAT Center for Interface Science and Catalysis, Department of Chemical Engineering, Stanford University, Stanford, California 94305, United States

[b] SUNCAT Center for Interface Science and Catalysis, SLAC National Accelerator Laboratory, Menlo Park, California 94025, United States

[c] Department of Materials Science and Engineering, Stanford University, Stanford, California 94305, United States

[d] SLAC National Accelerator Laboratory, Menlo Park, California 94025, United States

[e] Faculty of Science and Engineering, Manchester Metropolitan University, Manchester M1 5GD, United Kingdom

* Email: agallo@slac.stanford.edu, l.king@mmu.ac.uk, jaramillo@stanford.edu

Abstract

Reducing precious metal content and improving efficiency of proton exchange membrane (PEM) water electrolyzers is critical to produce renewable hydrogen cost effectively. Mixed metal iridium oxide catalysts (AIr_xO_y, A = non-precious metal) have demonstrated superior oxygen evolution reaction (OER) activity relative to IrO_2 catalysts while utilizing less Ir. However, improved stability is required if these materials are to be implemented commercially. In this work, we use a combination of *ex-situ* and *in-situ* characterization techniques to study physical and electronic properties of $Y_2Ir_2O_7$ as it evolves during OER in acidic electrolyte. We identify and quantify dissolution of Y and Ir, finding that this material exhibits similar stability to other reported mixed metal Ir oxides (10^4-10^5 $mol_{O2\ evolved}$/ $mol_{Ir\ dissolved}$) and appears to become more stable over time. We find that the catalyst surface becomes enriched with Ir after electrochemical testing. We further monitored the Ir oxidation state *in-situ* using high-energy resolution fluorescence detected x-ray absorption spectroscopy (HERFD-XAS). Our results suggest that the Ir oxidation state is dynamic: an IrO_x surface forms that is more oxidized than the bulk pyrochlore material but subsequently dissolves. Such detailed characterization of material properties can be used to develop design principles for improving catalyst stability.

Introduction

H_2 produced from proton exchange membrane (PEM) electrolysis is a promising route to decarbonize H_2 in existing and emerging markets of the global economy.[1] However, PEM electrolysis is still prohibitively expensive for most H_2 markets today.[2] One pathway to help reduce this cost is to develop lower cost, more active, and more stable catalysts for the oxygen evolution reaction (OER). Today, high mass loadings of Ir, an expensive precious metal, are utilized in commercial PEM electrolyzers.[3] While not the most active OER catalyst, IrO_x is practically the only material stable enough to oxidize water in an acidic environment on a years-long timescale.[3,4] Altering the composition of Ir-containing materials has been proposed as a method to improve intrinsic OER activity and stability in acidic electrolytes.[5–7]

Previous work has shown that mixed metal Ir oxides (AIr_xO_y) can achieve higher initial intrinsic activity than IrO_2 catalysts.[8–10] However, this is not true of all AIr_xO_y compositions. For example, in one report, $Y_2Ir_2O_7$ was shown to have 3x greater current density at 1.525 V vs. RHE than IrO_2 when normalized by the surface area of the catalyst, while other compositions ($A_2Ir_2O_7$, A = Bi, Pb) did not yield the same level of enhancement over IrO_2.[8] Similarly, another series of $A_2Ir_2O_7$

(A = Yb, Gd, Nd) was evaluated for OER, where only $Yb_2Ir_2O_7$ exhibited greater activity than a rutile IrO_2 at 1.58 V vs. RHE.[10] These results highlight that factors such as the initial catalyst composition can greatly impact the observed activity of these materials.

While it is common to relate initial composition to OER activity, the initial composition may evolve under OER operating conditions. As evidence of this evolution, not only do some AIr_xO_y compositions exhibit greater initial intrinsic activity relative to IrO_2, but performance can actually improve over time during electrochemical testing.[8,9,11] One explanation for this activity improvement over time is by the leaching of the non-precious metal A-site from AIr_xO_y materials during OER in acidic electrolytes. It has been proposed that the leached A-site leaves behind an IrO_x surface structure, which is predicted to have high OER activity.[8,9]

Surface IrO_x layers on AIr_xO_y after OER in acidic electrolytes have been observed with *ex-situ* characterization methods. For example, $SrIrO_3$ and $IrNbO_x$ thin films and $BaIrO_x$ nanoparticles have shown the presence of highly disordered IrO_x surface layers (depleted of Sr, Nb, and Ba) and surface roughening after OER testing.[12–14] It is still unclear, however, if the IrO_x surface layer is universal to all AIr_xO_y compositions, or if the initial composition can impact the formation and stability of this surface layer. *In-situ* characterization methods to monitor local structural and electronic environment of Ir in these materials can help build fundamental understanding of such dynamic catalysts.

In this work, we conduct a detailed investigation into the OER activity and stability of nanoparticulate $Y_2Ir_2O_7$ in acidic electrolyte using a combination of electrochemical and advanced material characterization techniques. To this end, we synthesize a nanoparticulate $Y_2Ir_2O_7$ catalyst and use *in-situ* high-energy resolution fluorescence detected x-ray absorption spectroscopy (HERFD-XAS) to monitor the Ir oxidation state as dissolution occurs during OER. We also probe the catalyst surface using high resolution transmission electron microscopy (HR-TEM) and x-ray photoelectron spectroscopy (XPS) to characterize the catalyst structure and composition *ex-situ*. The combination of such *in-situ* and *ex-situ* experimental techniques facilitates improved fundamental understanding of catalyst activity and stability, leading to the next iteration of high-performing catalyst materials.

Experimental Methods

Materials

All chemicals and materials were used as received. Iridium chloride hydrate ($IrCl_3.xH_2O$, 99.9% purity, Aldrich), yttrium nitrate hydrate ($Y(NO_3)_3.xH_2O$, 99.9% purity, Spectrum Chemicals), and sodium nitrate ($NaNO_3$, 99.0% purity, Sigma Aldrich) were used as to synthesize the $Y_2Ir_2O_7$ catalyst. Iridium oxide (IrO_2, 99.9% purity, Aldrich), iridium metal powder (Ir, 325 mesh, 99.9% purity, Alfa Aesar), iridium chloride hydrate ($IrCl_3.xH_2O$, 99.9%, Aldrich) were used as standards for Ir oxidation state comparison. Ir black (Premetek, 55-65 m^2/g) was used to validate the HERFD-XAS experimental setup. Vulcan carbon (Vulcan XC 72, Fuel Cell Store) was used as the catalyst support during electrochemical testing. IPA (99.99%, HPLC grade, Fisher Chemical) was used as a solvent in the catalyst ink, and Nafion perfluorinated resin (10 wt% in H_2O, Sigma-Aldrich) was used as a binder in the catalyst ink. All catalyst inks were tested on polished glassy carbon disks or gold disks (5 mm diameter). Electrolytes were prepared from concentrated perchloric acid ($HClO_4$, 70% concentration, double distilled, GFS Chemicals) and concentrated sulfuric acid (H_2SO_4, 99.999% purity, Aldrich). A graphite rod (< 2 ppm impurities, Ted Pella) was used as the counter electrode and the electrolyte was continuously purged with oxygen gas (99.993% purity) during electrochemical tests.

Pyrochlore Synthesis

Catalyst synthesis was based on previous reports for nanoparticulate $Y_2Ir_2O_7$.[8] Iridium chloride (105 mg) and yttrium nitrate (136 mg, 1.2:1 molar ratio Y:Ir) were dissolved in 10 mL of water. Sodium nitrate (2.5 g) was added to the solution, then the solution was heated to 80ºC while stirring to evaporate the liquid (~7 hr). The resulting dark green sludge was further dried in an oven at ~80ºC overnight. The solid was collected and ground using a mortar and pestle for 2 minutes, then transferred to an alumina combustion boat. The solid was heated in air, ramping from room temperature to 150ºC at a rate of 1ºC/min, held at 150ºC for 30 min, then heated to 550ºC at a rate of 2ºC/min where it was held for 2 hr. The sample cooled to <50 ºC in the furnace before removing. The resulting material formed a hard layer in the bottom of the combustion boat, which required using a metal spatula and water to extract into a centrifuge tube. Additional water (20 mL) was added to disperse the solid, and the mixture was centrifuged (1200 rpm, 5 min) to separate the solid particles. The water was decanted, and this process was repeated 2 more times. Finally, the collected particles were dried overnight at 80ºC to remove residual water.

Material Characterization

X-Ray Diffraction (XRD)

X-ray diffraction (XRD) of the as-prepared pyrochlore powder and Ir standard powders was performed using a Bruker D8 Venture with Mo Kα radiation to determine crystallinity. Diffraction patterns from the Mo Kα radiation were shifted to Cu Kα radiation using Bragg's law. XRD of the catalyst after electrochemical testing was performed using a PANanalytical XPert with Cu Kα radiation at a grazing incidence angle to enhance the catalyst signal relative to the substrate. The measured XRD pattern were matched to a $Y_2Ir_2O_7$ reference pattern from the ICSD database: 04-002-4000.

Scanning Electron Microscopy (SEM)

A Thermo Fisher Scientific Apreo S LoVac was used to perform scanning electron microscopy (SEM) on as-synthesized $Y_2Ir_2O_7$ nanoparticles. A 5 kV and 50 pA electron beam was used at a working distance of 5 mm. The sample was prepared by grinding nanoparticles into a clean aluminum pin stub mount (Ted Pella).

X-Ray Photoelectron Spectroscopy (XPS)

XPS was performed on a PHI Versaprobe 3 with Al Kα radiation to determine composition and elemental oxidation state. Powder samples and glassy carbon disks were mounted onto the sample holder using double-sided carbon tape. All XPS data sets were analyzed using CasaXPS software. High resolution scans were aligned to the C 1*s* peak (284.8 eV) arising from adventitious carbon. Ir 4*f* and Y 3*d* doublets were fit assuming proportional peak areas and the same full width half max. The peak splitting of the doublets was allowed to vary, but in all cases the fit peaks were in agreement with the reported peak splitting values for Ir and Y. Neither charge neutralization nor sputtering were performed during data collection. We found that charge neutralization did not change the Ir peak positions, and sputtering, while useful to remove Nafion and carbon, was avoided so as not to disturb the surface of the catalysts or reduce the oxides.

BET (Brunauer, Emmett, and Teller) Surface Area

The BET surface area of the as-prepared catalyst powder was measured using a Quantachrome Autoflow BET+. The sample (80 mg) was first degassed in a series of heating steps at 80ºC, 120ºC, and 150ºC, holding each for 30 min and heating at a rate of 2ºC/min between the steps. The final degas step occurred at 200ºC, which was held for 90 min. A 9-point BET measurement was conducted in a bath of liquid nitrogen and using nitrogen gas as the adsorbate.

Transmission Electron Microscopy (TEM)

Scanning transmission electron microscopy with energy dispersive x-ray spectroscopy (STEM-EDS) was performed using a FEI Titan Environmental TEM 80-300 operated at 300kV with a probe size of 0.3 nm to map elemental composition of the catalysts. Spatial resolution of the STEM-EDS mapping result is estimated to be ~4 nm. High-resolution TEM images were taken using the same instrument operated at the same high tension, the TEM is also equipped with an image corrector. Samples were prepared by sonicating the catalyst ink-coated substrates in IPA for 1 min, then depositing 3 drops of the solution onto lacey carbon TEM grids with Cu mesh.

X-Ray Absorption Spectroscopy (XAS)

All x-ray absorption spectroscopy was performed at the Stanford Synchrotron Radiation Lightsource (SSRL) at SLAC National Laboratory. *Ex-situ* high-energy resolution fluorescence detected x-ray absorption spectroscopy (HERFD-XAS) measurements at the Ir L_{III}-edge (∼11.2 keV) were collected at beamline 6-2 (0.15×0.4 mm^2 spot size, 3×10^{12} photon/s) in fluorescence mode averaging 4-6 scans of the samples at ambient temperature and pressure.[15] The Ir metal and $IrCl_3$ reference powders (2-3 mg) were pelletized with boronitride powder (1.0 g). *Ex-situ* IrO_2, Ir black, and $Y_2Ir_2O_7$ samples were collected before *in-situ* measurements. Description of *in-situ* sample preparation is below. *Ex-situ* Ir L_{III}-edge (∼11.2 keV) XAS was also conducted at SSRL's beamline 9-3 (1×4 mm^2, 2×10^{12} photon/s), which has lower energy resolution than the HERFD-XAS conducted at beamline 6-2. Data analysis was performed by aligning, averaging, and normalizing the collected spectra using the Athena software.[16] The peak position was determined by the x-intercept (or zero value) of the 1st derivative of the XAS spectra.

In-situ HERFD-XAS measurements at the Ir L_{III}-edge (∼11.2 keV) were conducted at SSRL's beamline 6-2. Samples were prepared by first pyrolyzing the catalyst substrate, a Kapton film (2 mil thick) between two graphite plates at 1000ºC for 1 hr in N_2. Catalyst inks were then deposited onto the pyrolyzed Kapton film substrate (10 $\mu g_{Ir}/cm^2_{geo}$), which was epoxied over a hole (0.65 cm diameter) in a high-density polyethylene bottle. The deposited catalyst was in contact with O_2-sparged 0.5 M H_2SO_4 electrolyte in the bottle, while the back of the film was exposed to air and contacted with Cu tape.

Electrochemical data for the *in-situ* experiments was recorded with a Biologic SP-300 potentiostat. Electrochemical performance was assessed using a 3-electrode configuration with a graphite counter electrode and Hg-$HgSO_4$ reference electrode inserted through the bottle cap. This experimental setup was largely modelled after Ref. 17, where schematics of the setup can be found. Measurements were conducted in the back side illumination configuration using the seven crystal Johann-type hard x-ray spectrometer developed on beamline 6-2 at SSRL.[15] XAS measurements were collected at a range of oxidative electrochemical potentials and the electrolyte was collected after the experiments for ICP-MS analysis. Data analysis was performed by aligning, averaging, and normalizing the collected spectra using the Athena software.[16]

Electrochemical Characterization

Electrode Preparation

Catalyst inks were prepared by dispersing the catalyst (3.5 mg) and Vulcan carbon (3.5 mg) in a solution of IPA (2.4 mL) and water (7.6 mL), following a published protocol.[18] Inks were iced for 5 min before adding Nafion ionomer (40 µL, D520 dispersion, 5wt%). All inks were sonicated for 20 min, iced for 5 min, then horn sonicated in a pulse profile (5 s on, 2 s off, 50% amplitude) for 2 min immediately before use. Inks were drop cast onto the substrate (in 8 µL increments) while rotating the electrode (100 rpm) inside a fume hood until the surface was visibly dry (~20 min).

Rotating Disk Electrode (RDE) Electrochemical Measurements

The OER performance of each catalyst was assessed in O_2-purged 0.1 M $HClO_4$ or 0.5 M H_2SO_4 electrolyte (50 mL) using a three-electrode configuration with a graphite counter electrode and Ag-AgCl reference electrode. A rotating disk electrode (RDE) configuration and BioLogic VMP3 potentiostat were used for all electrochemical tests unless otherwise noted.

Electrodes for activity measurements were prepared by depositing catalyst ink (14.3 μL for $Y_2Ir_2O_7$, 18 μL for Ir-IrO_x) onto a glassy carbon disk substrate (0.196 cm^2) resulting in a catalyst loading of ~15 $\mu g_{Ir}/cm^2_{geo}$ (57wt% Ir in $Y_2Ir_2O_7$; 86wt% Ir in Ir-IrO_x). The OER activity was assessed using cyclic voltammetry (CV) where the potential was cycled between 1.3 V and ~1.6 V vs. RHE (the potential required to reach a current density of ~10 mA/cm^2_{geo}) at a scan rate of 10 mV/s. This scan rate is within the range of scan rates recommended in OER catalyst benchmarking protocols[18] and used by others in the field.[10] Additional OER activity assessments using sequential voltage holds at 1.4, 1.5, 1.55, 1.6, and 1.63 V vs. RHE for 5 min each. Double layer capacitance measurements using CVs (0.66-0.86 V vs. RHE) at 300, 200, 100, 50, 20, and 10 mV/s scan rates were also used to assess changes in electrochemically active surface area. Impedance measurements were conducted at open circuit potential prior to electrochemical measurements and all measurements were corrected for the Ohmic resistance of the electrolyte after testing (0% compensation during testing).

Electrodes for chronoamperometry (CA) stability measurements were prepared by depositing 43 μL of $Y_2Ir_2O_7$ catalyst ink onto a gold disk substrate (0.196 cm^2) resulting in a total catalyst loading of ~75 $\mu g/cm^2_{geo}$. Gold substrates have demonstrated greater resistance to degradation during OER testing in acid than glassy carbon disks and therefore mitigate substrate degradation when evaluating system degradation mechanisms and quantifying catalyst dissolution.[19,20] The applied voltage was corrected for 85% of the Ohmic resistance of the electrolyte during the experiment using impedance measurements at open circuit voltage prior to beginning the experiment. Stability was also assessed using chronopotentiometry (CP) at a constant current of 0.38 mA (~2 mA/cm$^2_{geo}$). In this experiment, 30 ug$_{cat}$/cm$^2_{geo}$ was deposited onto a glassy carbon substrate.

Electrolyte Characterization

Inductively coupled plasma mass spectrometry (ICP-MS) was performed using a Thermo Scientific XSERIES 2 to quantify dissolved catalyst in the electrolyte. Electrolyte aliquots (4 mL) were taken periodically during stability experiments for ICP-MS analysis and fresh electrolyte (4 mL) was replenished such that the total volume of electrolyte (50 mL) was unchanged. Millipore water (4 mL) was added to each aliquot to achieve the minimum volume required for ICP-MS analysis. ICP-MS calibration standards were prepared using serial dilutions of commercial stock solutions. Quality control samples were prepared independently using the commercial stock solutions. The lowest reliable quantification limit for the dissolved mass fraction of each element was determined based on the catalyst loading, electrolyte volume, standard calibration curves, and baseline ion counts in solution: $\sim$1% for Y and Ir. In other words, we were able to reliably quantify dissolution if > 1% of the total Ir in the catalyst dissolved into the electrolyte, for example.

S-Number Calculation

The stability number (S-number) was used to quantify stability, normalizing the activity of the catalyst (moles of O_2 evolved) by the dissolution of Ir (moles of Ir dissolved). The amount of O_2 evolved was determined by integrating the current (I) divided by Faraday's constant (F) and the number of moles of electrons required to make a mole of O_2 (n) over time. This cumulative value of O_2 evolved was normalized by the concentration of Ir in the electrolyte at that time point (C_{Ir}^t)

times the volume of the electrolyte (V). We assume 100% Faradaic efficiency for OER in our calculations.

$$S - number = \frac{mol_{O2\ evolved}}{mol_{Ir\ dissolved}} = \frac{\int \frac{I}{Fn}\, dt}{C_{Ir}^{t} V} \qquad (1)$$

Results and Discussion

Nanoparticulate, crystalline $Y_2Ir_2O_7$ with highly oxidized Ir sites

We employed a modified Adams Fusion method to synthesize crystalline $Y_2Ir_2O_7$, which has been previously reported to yield high surface area Ir pyrochlore nanoparticles.[8] Using XRD, we confirmed the bulk crystallinity and phase purity of the as-synthesized catalyst by comparing the measured pattern to a reference pattern for $Y_2Ir_2O_7$ in the ICSD database (**Figure 1A**). Using XPS to compare the atomic concentration of Y and Ir, the as-prepared catalyst was found to be slightly Y enriched in the near-surface region (1.1:1 Y:Ir molar ratio) (**Figure S1**). The measured BET surface area of the $Y_2Ir_2O_7$ powder was 22 m^2/g (C-value of fit = 241). Imaging the particles with SEM revealed an average particle size of ~50 nm (**Figure S2**). Given this particle size, only a small fraction of the total atoms in the nanoparticle are at or near the surface. As a result, in bulk material characterization techniques such as XRD and XAS described further below, we expect only a small fraction of the signal to come from surface atoms.

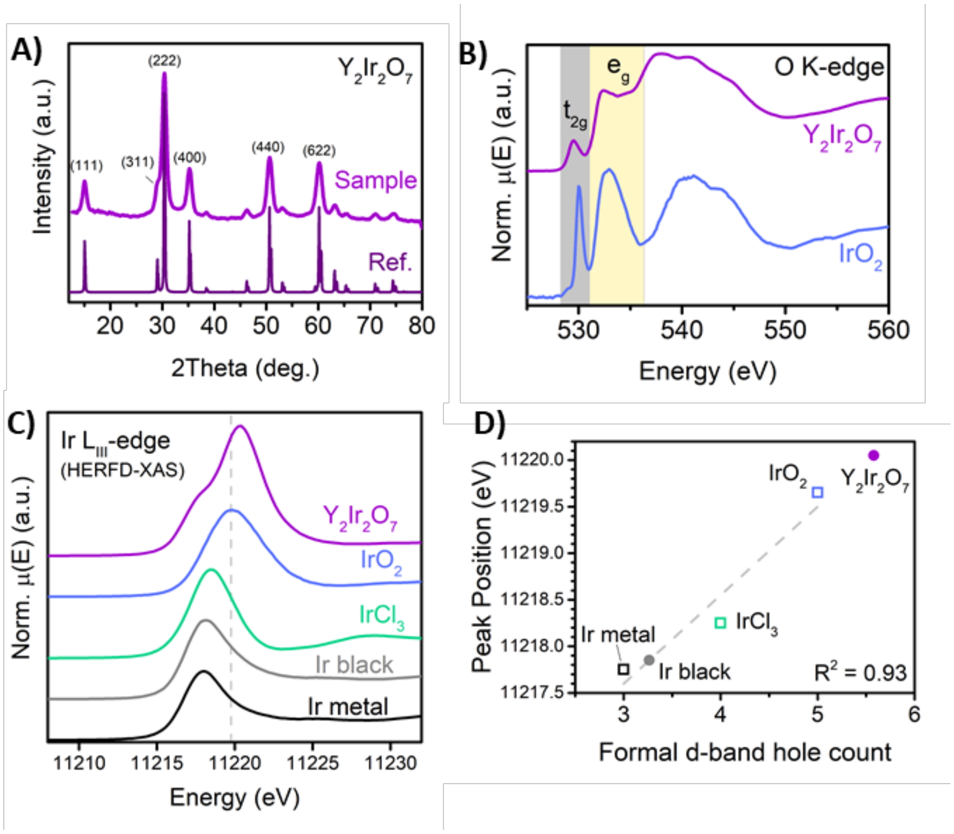

Figure 1. (A) XRD pattern for as-synthesized $Y_2Ir_2O_7$ matches reference XRD pattern from the ICSD database. (B) Normalized O K-edge XAS of $Y_2Ir_2O_7$ and IrO_2 with the Ir 5d t_{2g} and e_g regions highlighted in gray and yellow, respectively. (C) HERFD-XAS of the Ir L_{III}-edge of samples and standards. Vertical light gray dotted line through IrO_2 peak guides the eye. (D) HERFD-XAS Ir L_{III}-edge calibration curve. Linear fit of standard materials (open squares). The formal *d*-band hole count for Ir black and $Y_2Ir_2O_7$ samples (solid circles) estimated based on linear fit calibration curve (slope = 0.89 eV per *d*-band hole).

The extent of O 2*p*-Ir 5*d* orbital hybridization was characterized using O K-edge XAS (**Figure 1B**). The features at 529 and 532 eV arise from the excitation of a core O 1*s* electron to an O 2*p* orbital hybridized with Ir 5*d* t_{2g} and e_g orbitals.[21] The larger intensity of these features for the IrO_2 suggest a greater interaction between the Ir 5*d* and O 2*p* orbitals than in $Y_2Ir_2O_7$. This result is expected as $Y_2Ir_2O_7$ has lower electrical conductivity than IrO_2, and similar results have been observed for $A_2Ir_2O_7$ (A = Pr, Nd, Gd, Tb, Ho).[22]

High-energy resolution fluorescence detected x-ray absorption spectroscopy (HERFD-XAS) at the Ir L_{III}-edge was also used to determine the average Ir oxidation state across the surface and throughout the bulk of the as-prepared material (**Figure 1C**, **Figures S3-S4**). The peak position of the reference materials (Ir metal: $5d^7 6s^2$, $IrCl_3$: $5d^6 6s^0$, IrO_2: $5d^5 6s^0$) show a linear relationship with formal *d*-band hole count (**Figure 1D**, slope = 0.89 eV per *d*-band hole), which is considered a measure of oxidation state.[23] Previous reports have also shown that a unit change in oxidation state (+/- 1) correlates with a shift of ~1 eV. By extrapolating the linear regression, $Y_2Ir_2O_7$ has a formal *d*-band hole count of 5.6 (greater than the 5.0 *d*-band holes for IrO_2), indicating that $Y_2Ir_2O_7$ has mixed $Ir^{IV+/V+}$ states and is generally more oxidized than the Ir^{IV+} in the IrO_2 reference. This high oxidation state is also consistent with high resolution XPS measurements of the Ir 4*f* region (**Figure S5**). Fitting the Ir 4*f* region also reveals a greater relative amount of screened than unscreened 4*f* orbital character in $Y_2Ir_2O_7$ compared to IrO_2.[8,24–27]

The HERFD-XAS spectra for $Y_2Ir_2O_7$ shows a peak with a shoulder feature (~11,218 eV) as opposed to IrO_2 which shows a single smooth peak (**Figure 1C**). This shoulder feature does not change with consecutive individual scans, suggesting that it is not an artifact of beam damage from the high photon flux of the measurement (**Figure S4**). We note that this shoulder feature can be subtle (and even go unnoticed) when the Ir L_{III}-edge spectra is collected with standard resolution, and is not always reported for $Y_2Ir_2O_7$ or other AIr_xO_y materials.[6,8,14,24,28,29] To prove this, we collected Ir L_{III}-edge XAS on the same material using a beamline with standard resolution and did not observe the same clear splitting of the peak (**Figure S6**), consistent with previous reports showing the advantages of HERFD-XAS at the Ir L_{III}-edge.[30]

This distinctive peak shape measured by HERFD-XAS is attributed to the different electronic configuration of Ir in $Y_2Ir_2O_7$, where electron correlations and spin-orbit coupling are known to split the Ir 5d t_{2g} orbital into e'' and u' orbitals.[23,24,31,32] Whereas all five d valence electrons in IrO_2 occupy the t_{2g} orbital that spans the Fermi level, the d electrons in $Y_2Ir_2O_7$ fill the u' orbital and half-fill the higher energy e'' orbital with localized empty states above the Fermi level.[24,33] In addition, the intensity of the low energy shoulder feature in the white line strongly depends on the number of holes in the t_{2g} states, which is greater for $Y_2Ir_2O_7$ than IrO_2 as evidenced by the white line position (**Figure 1C**) and the XPS results (**Figure S5**).[27] In other words, the double feature we observed is due to the gap in t_{2g} states and the high oxidation state of Ir. This d-band structure gives rise to the electronically insulating property of $Y_2Ir_2O_7$ (compared to the more conductive IrO_2) and has been observed in other insulating AIr_xO_y materials.[33–35]

Electrochemical activity for OER improves with voltage cycling

The OER activity of $Y_2Ir_2O_7$ was assessed in 0.5 M H_2SO_4 electrolyte using cyclic voltammetry (CV) in an RDE (**Figure 2**). To put the activity of $Y_2Ir_2O_7$ in context, we provide a list of state-of-the-art Ir-based catalysts' OER activity in **Table S1**, including AIr_xO_y and Ir-Ti oxides. For reference, we also show CVs with the current normalized by BET surface area and geometric area (**Figure S7**), and assessed in 0.1 M $HClO_4$ in **Figure S8**. We acknowledge that CVs may over-state the performance of the catalyst, although this is a common method to assess performance in the field.[18] The performance was also assessed using a series of potential holds, which resulted in lower performance than a CV taken prior to the potential hold measurements. Interestingly, this performance was seemingly recovered after the potential holds (**Figure S9**). Further probing this phenomenon could be the subject of future work; here, we highlight that the catalyst is active and stable enough for further characterization.

Cycling the voltage, we found that the OER activity of $Y_2Ir_2O_7$, on a geometric area basis, improved with continual cycling, at least through 50 cycles. This improvement may be due to an increase in intrinsic catalytic activity,[9] and/or an increase in electrochemically active surface area (ECSA). We estimated the change in ECSA by employing the well-known CV method.[36] We found that the double layer capacitance of the electrode increased by ~3x after OER cycling compared to before cycling (**Figure S10**). Similar improvements in activity and increased double layer capacitance have been observed previously for AIr_xO_y materials when cycled repeatedly.[8,10] However, it is unclear whether the change in double layer capacitance is due to changes in the catalyst surface, or the Vulcan carbon support, which may be the subject of future investigation. For the purposes of this work, the $Y_2Ir_2O_7$ catalyst showed high mass-normalized activity and interesting stability, making it a suitable candidate for further electrochemical and material property characterization using *in-situ* measurements.

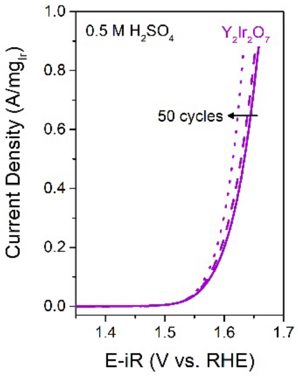

Figure 2. Oxidative sweep from cyclic voltammograms in 0.5 M H_2SO_4 electrolyte. 1st sweep (solid line), 10th sweep (dashed line), and 50th sweep (dotted line) for $Y_2Ir_2O_7$. Voltage scan rate of 10 mV/s. Current density normalized by initial mass of Ir in $Y_2Ir_2O_7$.

Chemically inert, but non-stoichiometric dissolution occurs during OER in acid

The chemical stability of OER catalysts in acidic environments is important for PEM electrolyzer applications. The stability of $Y_2Ir_2O_7$ in acid under no applied potential was assessed by soaking the catalyst as-deposited on an electrode in 0.5 M H_2SO_4. After 24 hr, less than 1 wt% of the Ir had dissolved, thus showing good chemical stability in acidic environments. Y dissolved in a greater amount (7 wt%), which suggests Y depletion from the catalyst surface occurred even before applying an electrochemical potential.

The electrochemical stability of $Y_2Ir_2O_7$ during OER was investigated by chronoamperometry (constant potential), during which electrolyte aliquots were taken for subsequent ICP-MS analysis. The experiment began with an initial linear sweep voltammogram (LSV) and open circuit voltage (OCV) hold for 20 min, followed by a potential hold at 1.6 V vs. RHE. A fixed potential was applied to control the thermodynamic driving force for catalyst dissolution (**Figure 3B**). However, we note that test conditions such as electrolyte, pH, and test protocol can influence catalyst dissolution rate.[37,38] Additional stability testing was conducted in 0.1 M $HClO_4$ following a chronopotentiometry protocol, and we further discuss the impact of those parameters on measured stability in the Supporting Information (**Figure S11**).

During the CA, the current density decreased substantially during the 2 hr hold at 1.6 V vs. RHE (**Figure 3B**). We suspect that this is due to corrosion of the carbon support[39,40] or formation of micro-bubbles that block the active sites of the catalyst.[38] Non-stoichiometric dissolution occurred during the CA, whereby a greater amount of Y dissolved relative to Ir, in agreement with previous reports of $Y_2Ir_2O_7$ OER stability in acid.[8] The Ir dissolution curve also flattens out as OER slows or ceases, suggesting that dissolution occurs mainly during OER (**Figure 3A**).

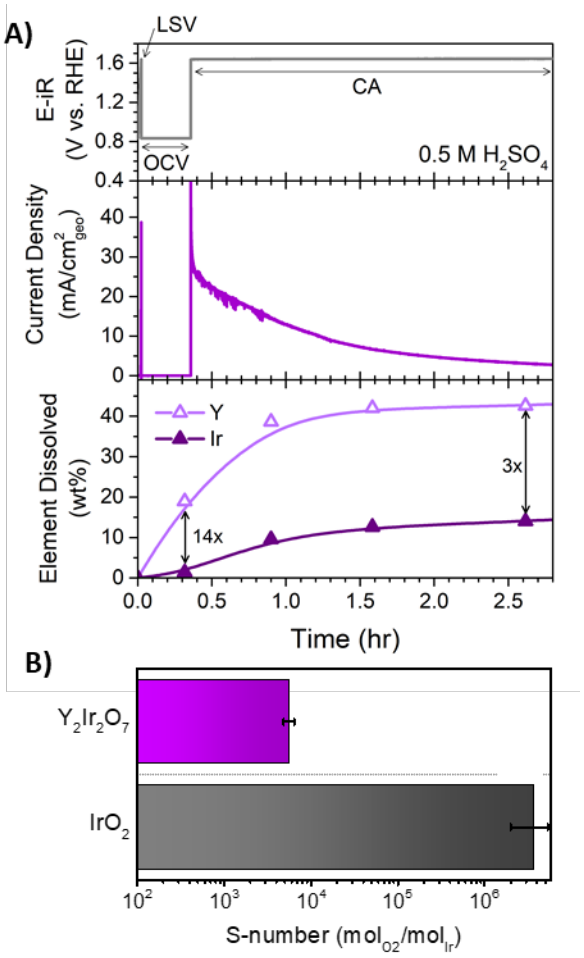

Figure 3. (A) Chronoamperometry (CA) experiment (1.6 V vs. RHE) of $Y_2Ir_2O_7$ in 0.5 M H_2SO_4. Amount of Y and Ir dissolved in electrolyte quantified by ICP-MS of electrolyte aliquots. (B) Average S-number for $Y_2Ir_2O_7$ evaluated in this work (purple bar) and IrO_2 powder evaluated by CP (range of 0.02 – 4 mA/cm$^2_{geo}$ for sequential 5 min holds) in 0.1 M $HClO_4$ from Ref. 41 (dark gray bar).

The stability number (S-number) was used to further quantify and compare stability, normalizing the activity of the catalyst (moles of O_2 evolved calculated from charge passed) by the dissolution of Ir (moles of Ir dissolved measured by ICP) (see Experimental Methods for details).[41] We note that the $Y_2Ir_2O_7$ catalyst investigated herein shows an average S-number (5.6×10^3 mol$_{O2}$/mol$_{Ir}$) close to that of other mixed metal Ir oxides ($AB_xIr_yO_z$) and amorphous IrO_x powders (**Figure 3B, Figure S11**).[41,42] The $Y_2Ir_2O_7$ catalyst studied in this work has an S-number that appears to increase with O_2 evolution, meaning that the catalyst seemingly gets more stable as it evolves more O_2 (**Figure S11**). This phenomenon has been observed for other AIr_xO_y catalysts,[41,42] but is not universal to all Ir-based catalysts.[41] Further discussion of this phenomenon, including the impact of experimental conditions such as pH, anions, and electrolyte flow rate is included in the Supporting Information. Ultimately, the S-number is still orders of magnitude lower than the reported stability of crystalline IrO_2,[41] but does highlight how tuning catalyst composition and structure can impact the rate of Ir dissolution during OER.

Bulk crystalline pyrochlore remains after testing

The CA experiment was conducted in modified triplicate, with each repeat experiment stopped after a different length of time to enable *ex-situ* characterization of the catalyst composition and morphology after varying amounts of degradation: after the OCV, after 30 min of CA, and after 2 hr of CA (**Figure 3A**).

XRD of the catalyst-coated substrate revealed that the bulk pyrochlore phase remained throughout the stability test (**Figure 4**). This corroborates our hypothesis that the substantial decrease in current in **Figure 3A** was not due to degradation of the bulk catalyst structure. Due to the low XRD signal, further information from the pattern, such as changes in relative peak intensities or widths, was not discernable.

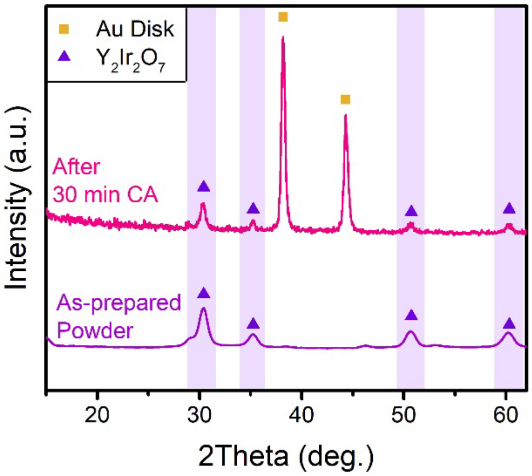

Figure 4. XRD patterns of as-prepared (fresh) $Y_2Ir_2O_7$ powder (purple pattern) and $Y_2Ir_2O_7$ on Au disk substrate after 30 min CA (pink pattern). $Y_2Ir_2O_7$ peaks highlighted with purple to draw attention.

XPS revealed that there was an increase in the relative amount of Ir present in the near-surface region of the catalyst after soaking in acid and electrochemical testing (**Table 1**). Furthermore, the near-surface composition appeared to reach a steady state (~40:60 Y:Ir molar ratio) after the single LSV+OCV prior to the start of the CA measurement at 1.6 V vs. RHE. Studies of similar AIr_xO_y materials have observed that an IrO_x surface layer forms during electrochemical testing as a result of A-site leaching and restructuring, which could explain the Ir-enrichment we observe by XPS.[43] Further analysis of the Ir oxidation state using high resolution XPS was conducted before and after stability testing, revealing small shifts (~0.3 eV) in the peak positions over time (**Figure S12**). However, to probe the Ir oxidation state during catalysis, we rely on *in-situ* characterization techniques described further below.

Table 1. Relative Y and Ir atomic concentrations from XPS.

Stage of Electrochemical Testing	Y:Ir Molar Ratio
As-deposited	52:48
After OCV	40:60
After 30 min CA	41:59
After 2 hr CA	41:59

The surface of the catalyst nanoparticles were further probed with high resolution transmission electron microscopy (HR-TEM) (**Figure 5**). Comparing the as-deposited and post-test samples, we did not find widespread, distinctive differences between the bulk crystallinity or edges/surface of the particles (**Figure 5A-F, Figure S13**). While there is no clear evidence by HR-TEM that an IrO_x surface layer formed after testing, we acknowledge that the *ex-situ* nature of the measurements (e.g., removing the electrochemical potential while in acid, etc.) could impact the surface morphology. In contrast, we did observe small nanoparticles (~1 nm diameter) as evidenced by the darker contrast within the lighter-colored carbon support (**Figure 5G-H, Figure S14**). These nanoparticles could be evidence of re-deposited IrO_x from the Ir that dissolved during testing, which has been hypothesized previously for Ir perovskite OER catalysts.[44] This would explain the discrepancy between the non-stoichiometric Y:Ir dissolution observed by XPS and ICP-MS and the lack of a visibly thick IrO_x surface layer in the HR-TEM images. XPS survey scans before and after testing also show no signs of contamination (**Figure S15**). The STEM-EDS mapping, however, had insufficient resolution to determine the composition of those small nanoparticles (**Figure S16**), thus identifying their composition and determining their contributions to OER catalytic activity should be the subject of a future investigation.

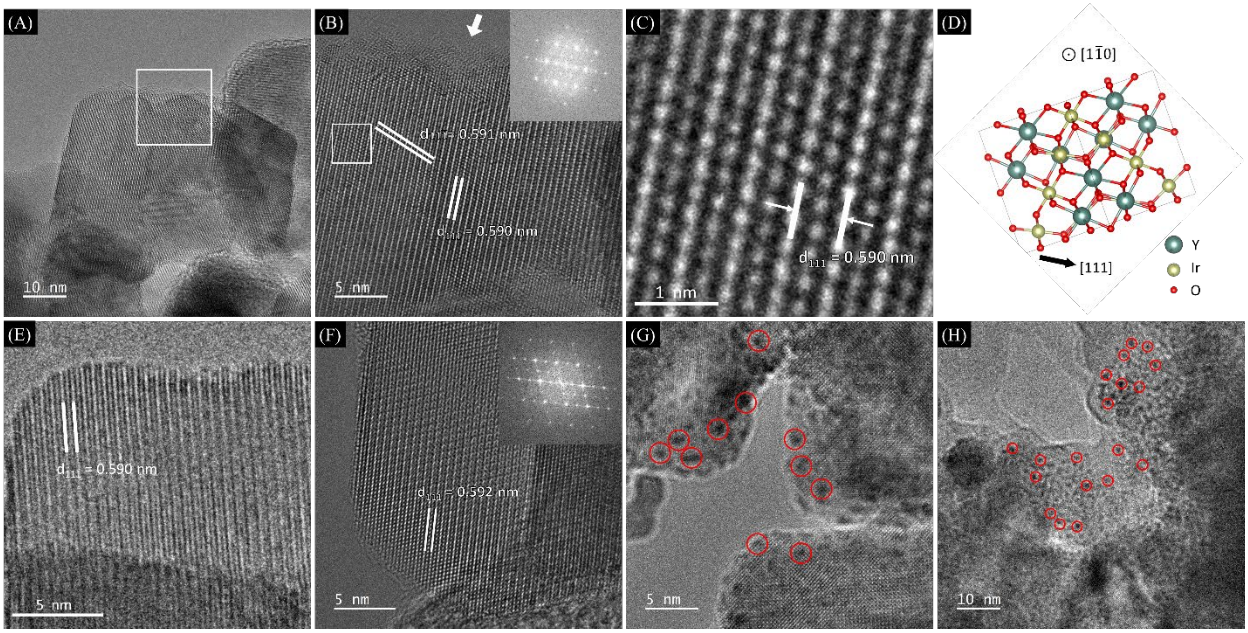

Figure 5. (A) HR-TEM of as-deposited catalyst. (B) Magnified image of the white outlined region in (A) showing the d-spacing corresponding to (111) crystal planes (**Table S2**); the inset FFT shows the particle is viewed along the [$\mathbf{1\bar{1}0}$] zone axis. (C) Magnified image of the white outlined region in (B) showing the alternating contrast corresponding to the atom arrangement along [111] direction as shown in (D). The white arrow in (B) points to surface with less ordered structure (more images showing particles with distinct surface can be found in **Figure S13-S14**). (E) HR-TEM images of nanoparticles after LSV+OCV period, and (F) after 30 min CA, both showing (111) crystal planes. TEM images in (G) and (H) also show the appearance of small nanoparticles (1-2 nm) for both tested particle catalysts, indicated by red circles.

In-situ **observation of Ir oxidation during dynamic OER and dissolution processes**

In-situ HERFD-XAS at the Ir L_{III}-edge was conducted to determine how the dissolution of Y from the catalyst affected the oxidation state of Ir during OER. We first measured the oxidation of a nanoparticulate Ir black catalyst (55-65 m^2/g) during OER to confirm that our *in-situ* experimental setup performed as expected. We stepped the potential from 1.1 V to 1.6 V vs. RHE, holding each potential for 20-25 min (enough time to collect 5-6 spectra) (**Figure S17**). As the potential increased, we observed a shift in the Ir L_{III}-edge peak position to higher energy by ~0.11 eV (**Figure S18**) and a clear broadening of the peak (**Figure S17**), suggesting that we were indeed observing the formation of surface IrO_x and validating our experimental setup.

For the $Y_2Ir_2O_7$ catalyst, we applied a constant potential of ~1.6 V vs. RHE in 0.5 M H_2SO_4 in order to compare the *in-situ* results with RDE measurements (**Figure 6A**). Over the course of the *in-situ* experiment, 20% of the Y and 4% of the Ir dissolved as quantified by ICP-MS of the electrolyte, indicating that the surface becomes Ir-enriched. This is a lower amount of dissolution than expected based on RDE measurements, but this could be the result of differences in the experimental setup (e.g., rotating vs. not-rotating electrode, type of substrate, catalyst loading, etc.).

When electrolyte was added to the cell at OCV, we observed a slight reduction in the Ir oxidation state relative to the *ex-situ* as-deposited sample before an electrochemical potential was applied (**Figure 6B-C**). The shift in the peak position corresponded to a +0.1 increase in the *d*-band hole count (**Figure S19-S20**). When a potential of 1.6 V vs. RHE was applied, the peak shifted to higher energies by +0.06 eV relative to the as-prepared sample, corresponding to an increased *d*-band hole count of ~0.06 (**Figure S20**). This result suggests Ir became more oxidized and the *d*-band hole count increased during OER relative to the as-deposited sample. We note that final oxidation state exhibiting Ir^{V+} character and the increase in oxidation state are consistent with *in-situ* XAS measurements for similar AIr_xO_y OER catalysts.[11,23,28] We further acknowledge that the magnitude of the increase shown here for $Y_2Ir_2O_7$ is smaller than those reports,[23] but we expect this difference is due to the higher initial Ir oxidation state in $Y_2Ir_2O_7$.

Similar *in-situ* XAS studies of IrO_2 and IrO_x catalysts have shown that the oxidation state of Ir can increase with electrochemical potential to Ir^{V+} or greater oxidation states.[45–47] In these studies, it was also observed that above the onset potential of OER, the oxidation state reaches a steady state[45] or even decreases.[46] We also note that theoretically, IrO_3 with Ir^{VI+} oxidation state is predicted to be more stable than rutile IrO_2 with Ir^{IV+} oxidation state under OER conditions.[48] The presence of such highly oxidized Ir such as $Ir^{V+/VI+}$ is reported to stabilize reactive oxygen species (O^{I-}), which is theorized to be responsible for the high OER activity of IrO_x catalysts.[49,50] By comparison, we suspect the highly oxidized Ir in $Y_2Ir_2O_7$ to have a similar effect on lattice oxygen, which could explain its high OER activity.

To observe how the Ir oxidation state changed over time as the catalyst performed OER and dissolved into the electrolyte, we held a constant potential (1.6 V vs. RHE) and measured consecutive scans (1.7 min each). We observed variation in the signal during this potential hold (**Figure 6C**), yet statistical analysis of the scans showed that the observed oxidation was detected beyond the noise in the as-deposited and OCV measurements. We therefore believe this to be a real phenomenon of the system, measurable due to the high resolution XAS measurements.

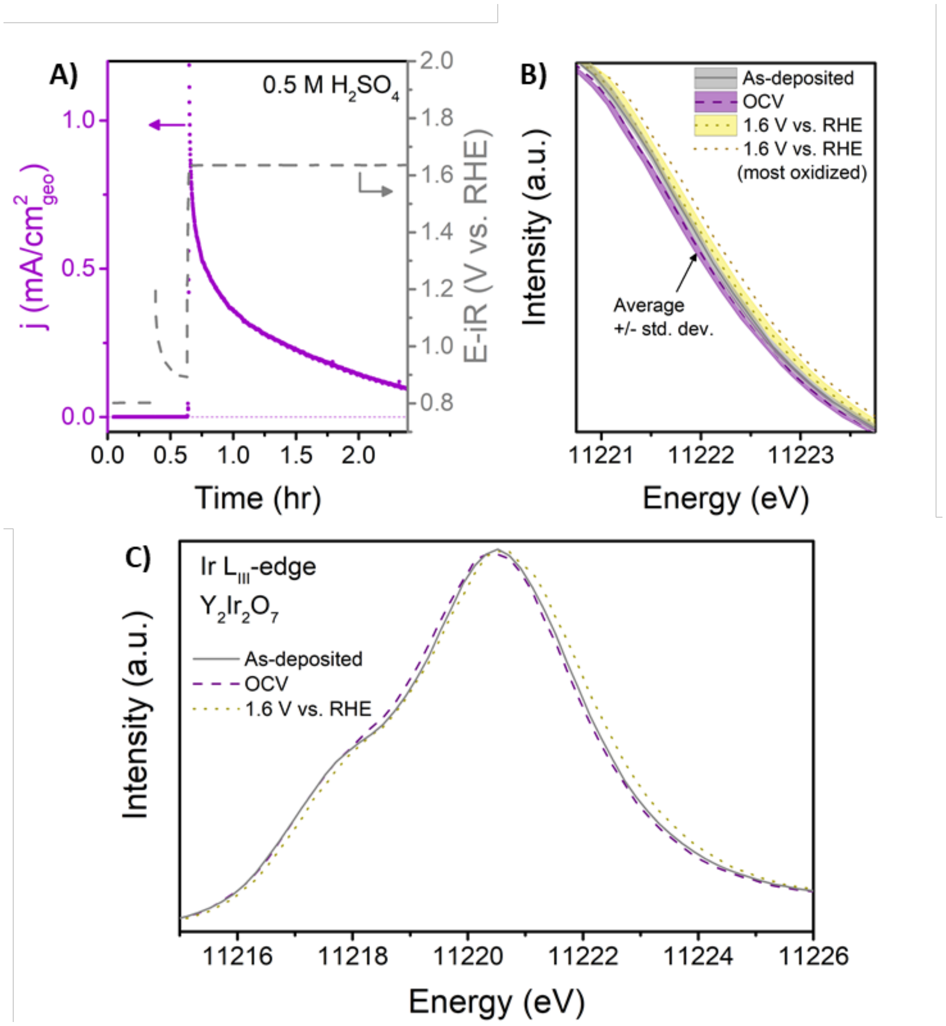

Figure 6. (A) Voltage profile (gray) and measured current density (purple) during *in-situ* measurements. (B, C) Ir L_{III}-edge HERFD-XAS spectra for $Y_2Ir_2O_7$ as-deposited (gray solid), at open circuit voltage (OCV, purple dashed), and the maximum oxidation measured during the 1.6 V vs. RHE potential hold (dotted gold). (B) Zoomed in region of (C), where colored shading was added to show standard deviation above and below average signal.

The surface of the $Y_2Ir_2O_7$ is dynamic under reaction conditions, both due to the oxygen evolution reaction and dissolution of Y and Ir. Our *ex-situ* XRD measurements confirm that the bulk $Y_2Ir_2O_7$ structure remains unchanged after testing (**Figure 4**), thus we would only expect to see Ir oxidation state changes at the surface. While this oxidation of surface Ir may be significant, given the size of the nanoparticles (50 nm), we only expect a small contribution to the total XAS signal from the surface Ir atoms. The variation in signal could be explained by a fluctuating Ir oxidation state on the catalyst surface: an increase in Ir oxidation state as Y leached from the structure forming an IrO_x surface layer, followed by a subsequent shift back towards the initial oxidation state as the IrO_x surface layer dissolved. The thickness of an IrO_x surface layer across all particles would vary at any given moment in time and would contribute to the signal fluctuations we observe. This could also explain why a thick surface IrO_x layer was not observed by TEM (**Figure 5**). Similar *in-situ* XAS studies of AIr_xO_y OER catalysts suggest that fluctuations in Ir oxidation state can also be explained by the relative A-site/O diffusion rates out of/into the IrO_x surface layer.[14] We find that this small, yet non-negligible, change in oxidation state is indicative of the relatively high stability of this Ir-based catalyst.

While the changes in the HERFD-XAS peak are clearly distinguishable (especially on the higher energy side of the spectra where there is less contribution from lower oxidation state Ir), we must acknowledge that the measured changes in both peak position and shape are approaching the resolution limit of our system. Future work to identify the surface Ir oxidation state of $Y_2Ir_2O_7$ using *in-situ* XAS could focus on further nanostructuring to increase the surface area of the catalysts to enhance the XAS signal arising specifically from surface Ir atoms.[51] Further, we acknowledge that our results are dependent on the specific OER potentials applied and electrolyte composition. Investigating Ir oxidation using *in-situ* HERFD-XAS as a function of electrolyte composition and electrochemical treatment could provide additional insight about $Y_2Ir_2O_7$ chemical and electrochemical stability. Such fundamental insight about electrochemical stability is critical in understanding the structural and electronic properties that yield high material stability in acidic, oxidizing conditions.

Conclusion

In summary, we quantified the dissolution of $Y_2Ir_2O_7$ as an OER catalyst, finding evidence of significant Y leaching and non-negligible Ir dissolution during OER in acidic electrolyte. Based on the S-number metric, we find that $Y_2Ir_2O_7$ has comparable stability to other reported mixed metal Ir oxides. Using *ex-situ* characterization techniques, we confirmed that an Ir-enriched material formed during electrochemical testing, yet the bulk crystalline structure and composition remained unchanged. We further found that the Ir oxidation stated appeared to increase and fluctuate during OER when monitored with *in-situ* HERFD-XAS at the Ir L_{III}-edge. We suspect that the fluctuations in the XAS spectra were caused by variations in thickness of a highly oxidized IrO_x surface layer that forms as Y dissolves, but then subsequently dissolves during OER. While this leaching catalytic material does not appear to improve the stability of highly active Ir sites for OER, continued efforts to extensively characterize material properties, quantify dissolution, and find descriptors for catalyst stability are needed to design the next generation of reduced precious metal OER catalysts for PEM electrolyzers.

Supporting Information Description

XPS and SEM of as-prepared nanoparticles; derivative of *ex-situ* HERFD-XAS; standard resolution XAS; OER activity of other Ir-based catalysts; additional OER activity metrics for $Y_2Ir_2O_7$ in 0.5 M H_2SO_4 and 0.1 M $HClO_4$; double layer capacitance; chronopotentiometry in 0.1 M $HClO_4$; discussion of S-number variation; $Y_2Ir_2O_7$ d-spacing values; HR-TEM, STEM-EDS, and XPS pre- and post-test; and HERFD-XAS calibration curve and derivatives for *in-situ* Ir black and $Y_2Ir_2O_7$

Raw data for all main text and supporting information figures

Acknowledgements

This research was supported by the U.S. Department of Energy, Office of Science, Office of Basic Energy Sciences, Chemical Sciences, Geosciences, and Biosciences Division, Catalysis Science Program to the SUNCAT Center for Interface Science and Catalysis. Physical characterization of the catalysts in this work was performed at the Stanford Nano Shared Facilities (SNSF), supported by the National Science Foundation under award ECCS-1542152. Juliet Jamtgaard is acknowledged for her support in XPS data interpretation. The authors acknowledge the Stanford University Environmental Measurements Facility and Guangchao Li for ICP-MS measurements. Use of Stanford Synchrotron Radiation Lightsource (SSRL), SLAC National Accelerator Laboratory is supported by the US Department of Energy, Office of Science, Office of Basic Energy Science, under Contract DE-AC02-76SF00515. The authors acknowledge the SSRL staff at beamline 9-3, specifically Matthew Latimer and Erik Nelson. McKenzie A. Hubert acknowledges the support of National Science Foundation Graduate Research Fellowship Program under Grant No. DGE-1656518. Any opinions, findings, and conclusions or recommendations expressed in this material are those of the author(s) and do not necessarily reflect the views of the National Science Foundation.

References

1. Staffell, I. *et al.* The role of hydrogen and fuel cells in the global energy system. *Energy Environ. Sci.* **12**, 463–491 (2019).

2. Mayyas, A., Ruth, M., Pivovar, B., Bender, G. & Wipke, K. *Manufacturing Cost Analysis for Proton Exchange Membrane Water Electrolyzers Manufacturing Cost Analysis for Proton Exchange Membrane Water Electrolyzers*. *National Renewable Energy Laboratory* **NREL/TP-6A20-72740**, (2019).

3. Ayers, K. *et al.* Perspectives on low temperature electrolysis and potential for renewable hydrogen at scale. *Annu. Rev. Chem. Biomol. Eng.* **10**, 219–239 (2019).

4. McCrory, C. C. L. *et al.* Benchmarking Hydrogen Evolving Reaction and Oxygen Evolving Reaction Electrocatalysts for Solar Water Splitting Devices. *J. Am. Chem. Soc.* **137**, 4347–4357 (2015).

5. Reier, T., Nong, H. N., Teschner, D., Schlögl, R. & Strasser, P. Electrocatalytic Oxygen Evolution Reaction in Acidic Environments - Reaction Mechanisms and Catalysts. *Adv. Energy Mater.* **7**, 1601275 (2017).

6. Sun, W. *et al.* A promising engineering strategy for water electro-oxidation iridate catalysts via coordination distortion. *Chem. Commun.* **55**, 5801–5804 (2019).

7. Regmi, Y. N. *et al.* Supported Oxygen Evolution Catalysts by Design: Toward Lower Precious Metal Loading and Improved Conductivity in Proton Exchange Membrane Water Electrolyzers. *ACS Catal.* **10**, 13125–13135 (2020).

8. Lebedev, D. *et al.* Highly Active and Stable Iridium Pyrochlores for Oxygen Evolution Reaction. *Chem. Mater.* **29**, 5182–5191 (2017).

9. Seitz, L. C. *et al.* A highly active and stable IrOx/SrIrO3 catalyst for the oxygen evolution reaction. *Science (80-.).* **353**, 1011–1014 (2016).

10. Abbott, D. F. *et al.* Design and Synthesis of Ir/Ru Pyrochlore Catalysts for the Oxygen Evolution Reaction Based on Their Bulk Thermodynamic Properties. *ACS Appl. Mater. Interfaces* **11**, 37748–37760 (2019).

11. Edgington, J., Schweitzer, N., Alayoglu, S. & Seitz, L. C. Constant Change: Exploring Dynamic Oxygen Evolution Reaction Catalysis and Material Transformations in Strontium Zinc Iridate Perovskite in Acid. *J. Am. Chem. Soc.* **143**, 9961–9971 (2021).

12. Spöri, C. *et al.* Molecular Analysis of the Unusual Stability of an IrNbOx Catalyst for the Electrochemical Water Oxidation to Molecular Oxygen (OER). *ACS Appl. Mater. Interfaces* **13**, 3748–3761 (2021).

13. Song, C. W., Suh, H., Bak, J., Bae, H. Bin & Chung, S. Y. Dissolution-Induced Surface Roughening and Oxygen Evolution Electrocatalysis of Alkaline-Earth Iridates in Acid. *Chem* **5**, 3243–3259 (2019).

14. Wan, G. *et al.* Amorphization mechanism of SrIrO3 electrocatalyst: How oxygen redox initiates ionic diffusion and structural reorganization. *Sci. Adv.* **7**, eabc7323 (2021).

15. Sokaras, D. *et al.* A seven-crystal Johann-type hard x-ray spectrometer at the Stanford Synchrotron Radiation Lightsource. *Rev. Sci. Instrum.* **84**, (2013).

16. Ravel, B. & Newville, M. ATHENA , ARTEMIS , HEPHAESTUS : data analysis for X-ray absorption spectroscopy using IFEFFIT. *J. Synchrotron Radiat.* **12**, 537–541 (2005).

17. Gibbons, B. M. *et al.* In Situ X-Ray Absorption Spectroscopy Disentangles the Roles of Copper and Silver in a Bimetallic Catalyst for the Oxygen Reduction Reaction. *Chem. Mater.* **32**, 1819–1827 (2020).

18. Alia, S. M. & Anderson, G. C. Iridium Oxygen Evolution Activity and Durability Baselines in Rotating Disk Electrode Half-Cells. *J. Electrochem. Soc.* **166**, F282–F294 (2019).

19. Geiger, S. *et al.* Catalyst Stability Benchmarking for the Oxygen Evolution Reaction: The Importance of Backing Electrode Material and Dissolution in Accelerated Aging Studies. *ChemSusChem* **10**, 4140–4143 (2017).

20. Yi, Y. *et al.* Electrochemical corrosion of a glassy carbon electrode. *Catal. Today* **295**, 32–40 (2017).

21. Suntivich, J. *et al.* Estimating Hybridization of Transition Metal and Oxygen States in Perovskites from O K-edge X-ray Absorption Spectroscopy. *J. Phys. Chem. C* **118**, 1856–1863 (2014).

22. Shang, C. *et al.* Electron Correlations Engineer Catalytic Activity of Pyrochlore Iridates for Acidic Water Oxidation. *Adv. Mater.* **1805104**, 1805104 (2018).

23. Nong, H. N. *et al.* A unique oxygen ligand environment facilitates water oxidation in hole-doped IrNiOx core–shell electrocatalysts. *Nat. Catal.* **1**, 841–851 (2018).

24. Shih, P.-C., Kim, J., Sun, C. & Yang, H. Single-Phase Pyrochlore Y2Ir2O7 Electrocatalyst on the Activity of Oxygen Evolution Reaction. *ACS Appl. Energy Mater.* **1**, 3992–3998 (2018).

25. Shang, C. *et al.* Electron Correlations Engineer Catalytic Activity of Pyrochlore Iridates for Acidic Water Oxidation - Supporting Info. *Adv. Mater.* 1805104 (2018). doi:10.1002/adma.201805104

26. Kawasaki, J. K., Uchida, M., Paik, H., Schlom, D. G. & Shen, K. M. Evolution of electronic correlations across the rutile, perovskite, and Ruddelsden-Popper iridates with octahedral connectivity. *Phys. Rev. B* **94**, 1–6 (2016).

27. Zhu, W. K., Wang, M., Seradjeh, B., Yang, F. & Zhang, S. X. Enhanced weak ferromagnetism and conductivity in hole-doped pyrochlore iridate Y2 Ir2 O7. *Phys. Rev. B - Condens. Matter Mater. Phys.* **90**, 1–7 (2014).

28. Burnett, D. L. *et al.* In situ XAFS of acid-resilient iridate pyrochlore oxygen evolution electrocatalysts under operating conditions. *Phys. Chem. Chem. Phys.* **22**, 18770–18773 (2020).

29. Antonov, V. N., Bekenov, L. V. & Kukusta, D. A. Pyrochlore iridates: Electronic and

magnetic structures, x-ray magnetic circular dichroism, and resonant inelastic x-ray scattering. *Phys. Rev. B* **102**, 195134 (2020).

30. Hoffman, A. S. *et al.* High-Energy-Resolution X-ray Absorption Spectroscopy for Identification of Reactive Surface Species on Supported Single-Site Iridium Catalysts. *Chem. – A Eur. J.* **23**, 14760–14768 (2017).

31. Maiti, K. Role of spin-orbit coupling and electron correlation in the electronic structure of a 5d pyrochlore, Y2Ir2O7. *Solid State Commun.* **149**, 1351–1355 (2009).

32. Feng, H. L. *et al.* Tl2Ir2O7: A Pauli Paramagnetic Metal, Proximal to a Metal Insulator Transition. *Inorg. Chem.* (2021). doi:10.1021/acs.inorgchem.0c03124

33. Krajewska, A. *et al.* Almost pure Jeff=1/2 Mott state of In2Ir2O7 in the limit of reduced intersite hopping. *Phys. Rev. B* **101**, 121101 (2020).

34. Pfeifer, V. *et al.* The electronic structure of iridium and its oxides. *Surf. Interface Anal.* **48**, 261–273 (2016).

35. Kim, Y.-J. *et al.* Probing electronic excitations in iridates with resonant inelastic x-ray scattering and emission spectroscopy techniques. *arXiv* 1–13 (2018).

36. Trasatti, S. & Petrii, O. A. Real surface area measurements in electrochemistry. *J. Electroanal. Chem.* **327**, (1992).

37. Arminio-Ravelo, J. A., Jensen, A. W., Jensen, K. D., Quinson, J. & Escudero-Escribano, M. Electrolyte Effects on the Electrocatalytic Performance of Iridium-Based Nanoparticles for Oxygen Evolution in Rotating Disc Electrodes. *ChemPhysChem* **20**, 2956–2963 (2019).

38. Hartig-Weiss, A., Tovini, M. F., Gasteiger, H. A. & El-Sayed, H. A. OER Catalyst Durability Tests Using the Rotating Disk Electrode Technique: The Reason Why This Leads to Erroneous Conclusions. *ACS Appl. Energy Mater.* **3**, 10323–10327 (2020).

39. Oh, H.-S. *et al.* Electrochemical Catalyst–Support Effects and Their Stabilizing Role for IrOx Nanoparticle Catalysts during the Oxygen Evolution Reaction. *J. Am. Chem. Soc.* **138**, 12552–12563 (2016).

40. Hubert, M. A. *et al.* Acidic Oxygen Evolution Reaction Activity-Stability Relationships in Ru-Based Pyrochlores. *ACS Catal.* **10**, 12182–12196 (2020).

41. Geiger, S. *et al.* The stability number as a metric for electrocatalyst stability benchmarking. *Nat. Catal.* **1**, 508–515 (2018).

42. Chen, Y. *et al.* Exceptionally active iridium evolved from a pseudo-cubic perovskite for oxygen evolution in acid. *Nat. Commun.* **10**, 572 (2019).

43. Chen, F., Wu, Z., Adler, Z. & Wang, H. Stability challenges of electrocatalytic oxygen evolution reaction: From mechanistic understanding to reactor design. *Joule* **5**, 1704–1731 (2021).

44. Zhang, R. *et al.* A Dissolution/Precipitation Equilibrium on the Surface of Iridium-Based Perovskites Controls Their Activity as Oxygen Evolution Reaction Catalysts in Acidic

Media. *Angew. Chemie Int. Ed.* **58**, 4571–4575 (2019).

45. Minguzzi, A. *et al.* Observing the oxidation state turnover in heterogeneous iridium-based water oxidation catalysts. *Chem. Sci.* **5**, 3591–3597 (2014).
46. Li, L. *et al.* Operando Observation of Chemical Transformations of Iridium Oxide During Photoelectrochemical Water Oxidation. *ACS Appl. Energy Mater.* **2**, 1371–1379 (2019).
47. Zheng, X. *et al.* Origin of enhanced water oxidation activity in an iridium single atom anchored on NiFe oxyhydroxide catalyst. *Proc. Natl. Acad. Sci.* **118**, e2101817118 (2021).
48. Flores, R. A. *et al.* Active Learning Accelerated Discovery of Stable Iridium Oxide Polymorphs for the Oxygen Evolution Reaction. *Chem. Mater.* **32**, 5854–5863 (2020).
49. Pfeifer, V. *et al.* Reactive oxygen species in iridium-based OER catalysts. *Chem. Sci.* **7**, 6791–6795 (2016).
50. Velasco-Vélez, J.-J. *et al.* Surface Electron-Hole Rich Species Active in the Electrocatalytic Water Oxidation. *J. Am. Chem. Soc.* **143**, 12524–12534 (2021).
51. Huang, H. & Russell, A. E. Approaches to achieve surface sensitivity in the in situ XAS of electrocatalysts. *Curr. Opin. Electrochem.* **27**, 100681 (2021).

Table of Contents Image